Near-field wire-based passive probe antenna for the selective detection of the longitudinal electric field at THz frequencies

Ronan Adam, Laurent Chusseau, Thierry Grosjean, Annick Pénarier, Jean-Paul Guillet, Daniel Charraut

Near-field wire-based passive probe antenna for the selective detection of the longitudinal electric field at terahertz frequencies

Ronan Adam,[1] Laurent Chusseau,[1,a)] Thierry Grosjean,[2] Annick Penarier,[1] Jean-Paul Guillet,[1] and Daniel Charraut[2]
[1]*Institut d'Électronique du Sud, UMR 5214 au CNRS, Université Montpellier 2, 34095 Montpellier, France*
[2]*Département d'Optique P.M. Duffieux, Institut FEMTO-ST, UMR 6174 CNRS, Université de Franche-Comté, 16 route de Gray, 25030 Besançon, France*

(Received 27 June 2009; accepted 31 August 2009; published online 12 October 2009)

A passive probe antenna for cw near-field microscopy at millimeter and submillimeter wavelengths is defined. It is based on the coupling between a free-space linearly polarized propagating beam to a wire mode. This is obtained efficiently owing to a discontinuous phase plate. This passive "optical" structure allows either the generation of a subwavelength confinement of the longitudinal electric field (polarized along the wire antenna) or, due to reciprocity, the collection of the longitudinal component of the electric field (along the wire antenna) with subwavelength resolution. The emission and collection properties of the proposed antenna have been demonstrated experimentally using a preliminary realization designed to work at 0.1 THz. Experimental results are well supported by calculations. © *2009 American Institute of Physics*. [doi:10.1063/1.3236665]

I. INTRODUCTION

Since its demonstration,[1] terahertz imaging has attracted high attention because of its high added value in spectroscopic applications especially considering biology or security (for a review, see Ref. 2). Going beyond the exploration of large uniform objects requires the application of near-field methods to overcome the diffraction limit. Following the way previously paved in the optical domain, it was demonstrated using an experimental apparatus derived from scanning near-field optical microscopy (SNOM) that terahertz near-field microscopy can be successful for high-resolution characterization at the nanometer scale of physical[3,4] or biological samples.[5] Only recently, the probe used for such experiments has been optimized and changed from the classic scattering tip.[6–8]

In the optical domain, Lee *et al.*[9] showed a polarization-resolved near-field imaging system with a nanometer-scale resolution using a modified SNOM scattering tip and an analyzer. This pioneer work has not been reproduced in the terahertz domain perhaps because it is difficult to transpose the detection scheme at these wavelengths where high quality polarizers, high-power illumination sources, and sensitive detectors are very expensive. In the millimeter-wave range, it was preferred to use dedicated probes that appeared in the early time of near-field characterization.[10] Longer wavelengths allow for easier probe fabrication and may serve to evaluate concepts to be transposed later at terahertz or optical frequencies. For example, probe developments have explored either antenna-based designs[11] or purely dielectric cones.[12] By successively scanning samples with various specific probes, it may be possible to discriminate the field components at its surface. Up to now, this task has been achieved in the terahertz domain by means of nonlinear optical materials for the emission[13] or the detection[14–18] of the radiations. For pure detection, these materials have the disadvantage of being of large size or being included in the sample itself. Henceforth, the resolution is limited by the trade-off between crystal size and sensitivity although it takes benefit from the ultimate vector sensitivity of nonlinear crystals. Therefore, antennalike probes seem to be much more promising to fulfill this objective.

A wire-based probe antenna dedicated to cw near-field microscopy at millimeter and submillimeter wavelengths has been defined and characterized. This passive device can generate either a subwavelength confinement of the longitudinal electric field (polarized along the wire antenna) or, due to reciprocity, it can mainly collect the longitudinal component of the electric field with subwavelength resolution. This scheme is different of near-field radiating tips because of the guiding and filtering properties brought by the Sommerfeld guided waves and the subsequent radiation of the signal in the far field for further detection.

In Sec. II, the wire-based probe antenna is detailed and theoretically discussed, then, in Sec. III, the emission properties of the structure are finely analyzed by imaging experimentally the two transverse components of the electric field (perpendicular to the wire). In Sec. IV, the study of the probe-to-probe coupling shows first the well-known wide extension in free space of the faintly localized surface plasmon polaritons along the wire,[19–21] and second the ability of the antenna to collect mainly the longitudinal component of the electric field. The latter property is confirmed in Sec. V through the near-field imaging of subwavelength square holes.

II. THE NEAR-FIELD PROBE ANTENNA

The principle of the system relies on the excitation of a radially polarized guided mode along a metal wire,[19] also known as a Sommerfeld wave (see Refs. 22–24). Note that special sources were already fabricated to efficiently match

a)Electronic mail: chusseau@univ-montp2.fr.

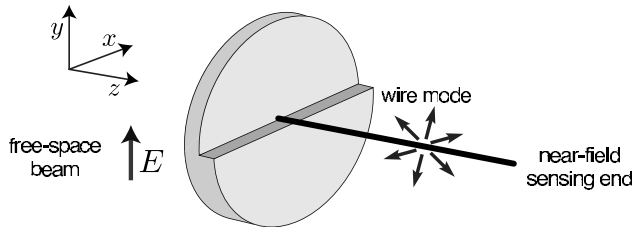

FIG. 1. Schematic of the passive near-field probe. A linearly polarized free-space propagating field can be efficiently converted in a radially polarized wire mode, and vice versa; thanks to a Teflon discontinuous phase element.

the radially distributed electric field of the wire mode.[25–27] In the present case, alternative ways of the Sommerfeld mode excitation are conducted. They originate from the emission and collection properties of the proposed near-field probe antenna and take benefit from the cw operating regime

The schematic of the antenna is given in Fig. 1. It consists of a metal wire directly connected to a discontinuous phase element (DPE). The DPE is a dielectric plate whose one interface exhibits a step and whose role is well known for the beam polarization management in order to generate cylindrical vector beams.[28,29] The step height of value $\lambda/2(n-1)$ (n is the index of refraction of the dielectric and λ is the wavelength) is chosen so that the field direction of a free-space input beam is inverted over the half of its cross section. When the step is orthogonal to the direction of the incident linear polarization, the input beam can efficiently couple to the wire eigenmode connected to it, and vice versa. The role of the DPE has already been validated in the development of a terahertz radial polarizer based on hollow circular metallic waveguides.[30]

The coupling between a free-space propagating beam and the wire mode can be finely estimated by calculating analytically the overlap integral between the incident field distribution and the radial coordinate of the guided electric field $E_r \propto H_1^{(1)}(\gamma r)$. Here, $H_1^{(1)}$ is the Hankel function of the first kind and $\gamma^2 = k^2 - h^2$, where $k = 2\pi/\lambda$, h is the propagation constant of the guided wave,[19] and r is the radial coordinate. A maximum efficiency of $\approx 40\%$ is calculated when coupling a Gaussian field with a π-phase shift on half of its incident plane to a wire guided mode field. It turns out that this coupling phenomenon depends mostly on the matching between the widths of the illuminating Gaussian beam and the wire mode, whereas the wire radius has a minor effect.

The radially polarized wire mode plays a central role in the electromagnetic interconnection between the wire subwavelength apex and the free-space far-field radiations. When the antenna is used in emission mode, a free-space linearly polarized beam is coupled to the wire mode through the DPE. The mode propagates toward the wire end, and due to the radial symmetry of the guided field, it leads to a longitudinally polarized subwavelength confinement just beyond the apex (polarized along the wire). The so-created longitudinal dipolelike emitter can be used as a nonradiative source for near-field optical applications. With the dipolelike source properly aligned perpendicularly to the sample average plane, no energy flow crosses the sample surface. By reciprocity, the extremity of the wire can play the role of a local collector of longitudinal electric field. In near-field collection mode, the longitudinal component of the three-dimensional (3D) electric field at a sample radiating surface can excite the wire mode, which propagates toward the DPE. Then, the DPE transforms the guided mode into a linearly polarized free-space propagating beam, which can efficiently couple to a detector through a rectangular waveguide or a horn antenna.

Because this technique requires only passive elements, it can be used with any kind of sources. Given the cutoff-free properties of the wire mode so excited, a tapered wire end can channel energy to a very confined zone located at the cone apex.[20,21,31] This superfocusing property is also known at optical frequencies[32] or for corrugated tips[33] that have a better guiding effect along the taper. By reciprocity, this kind of antennas can collect the signal in a tiny volume.

A preliminary passive antenna is built at 0.1 THz. It involves a 6 cm wide cylindrical DPE of polytetrafluoroethylene (or Teflon) with a step height of 3.5 mm. A small hole at the disk center is ground in order to insert and attach a bare tungsten wire normally to its surface. Two types of probe antennas are tested successively. First, the bare cylindrical wire is a simple tungsten wire of diameter 0.6 mm ($\lambda/5$) and length 12 cm. We also tried 4 cm long metal needles tapered over a distance of 5 mm up to a spike with a 2 μm radius of curvature. The latter needles were initially devoted to the electrical test of integrated circuits. The system is tested with an electronic cw source of ≈ 1 mW output power. In emission mode, the input Gaussian beam is resized with parabolic mirrors in order to optimize the coupling efficiency to the wire mode as theoretically predicted. In collection mode, the antenna is coupled to a horn antenna connected to the detector.

III. EMISSION MODE: TRANSVERSE FIELD MEASUREMENTS

The two-dimensional (2D) transverse electric field emitted by the probe antenna used in emission mode has been experimentally characterized. The sensor used for this experiment has a principle similar to that in Ref. 11. In practice, a 3 mm height pyramidal tip made of Teflon protrudes from the WR10 rectangular waveguide end. The two opposite largest facets of the tip are metal coated using Ni pulverization, and the sensitive end facet remains uncoated and exhibits dimensions of 20×40 μm^2. The second output of the WR10 waveguide is loaded by a Schottky diode that results in the direct measurement of the intensity collected by the pyramidal probe. Separate investigations have shown that this probe is sensitive only to the transverse electric field, the direction of which being given by the shortest dimension of the open rectangular WR10 waveguide.[34] As a consequence, when rotated by an angle of $\pi/2$, we can easily image two cross-rectangular polarizations. This probe will be named the analyzer in the sequel.

Figure 2 gives the characterization of the transverse field radiated by the probe antenna fabricated with the 12 cm long tungsten wire of 0.6 mm diameter. The two images of Figs. 2(a) and 2(b) were taken for the two cross polarizations of

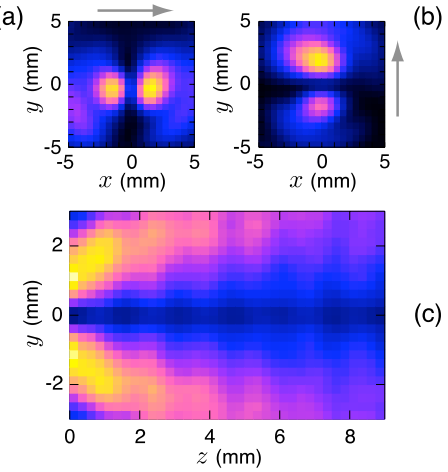

FIG. 2. (Color online) Transverse electric field as measured at the passive probe end located at the position $x=y=z=0$. [(a) and (b)] Transverse electric field measured in the (x,y)-plane normal to the wire at $z\approx 0$; the gray arrow indicates the polarization measured by the analyzer. (c) Vertical component of the electric field (located in the plane of the figure) measured in the (y,z)-plane.

the analyzer in the (x,y)-planes orthogonal to the wire, and as close as possible to the end of the metal wire, i.e., $z \approx 0.2$ mm. Remarkably, there is no transverse field at the center, and both images show similarly enhanced intensities regularly distributed at each side of the wire end. As expected, after a $\pi/2$-rotation of the analyzer, the obtained image is self-similar with the same $\pi/2$-rotation. This reveals the underlying symmetry of the radial field at the wire end in the transverse polarization, and a numerical reconstruction would have produced a doughnut for the total transverse intensity. Images are in full agreement with the expected radial field propagating along the wire.[19] The wire length of $\approx 40\lambda$ used in this experiment ensures that the wire mode is well established before leaving the wire. Consequently, it is expected that the transverse field exhibits a perfect axial symmetry around the wire. A slight asymmetry, however, appears in Figs. 2(a) and 2(b). This may be caused either by an imperfect alignment of the probe antenna with the input Gaussian beam or more certainly by a small bent of the 12 cm long thin wire in the (y,z)-plane owing to its own weight. As a matter of fact, the imaging planes were thus not rigorously orthogonal to the wire end, an effect that is obviously more important when imaging Fig. 2(b) than Fig. 2(a).

Additionally the electric field emitted at the wire end has been characterized in the vertical plane that includes the wire [Fig. 2(c)]. The measured intensity has been recorded for the y-polarization included in that vertical plane. The distance z between the wire end and the analyzer has been increased gradually up to 9 mm while scanning in the y vertical direction over ± 3 mm. Along with Figs. 2(a) and 2(b), it clearly shows that a radially polarized doughnut beam propagates in free space beyond the wire end located at $x=y=z=0$. The field intensity is measured at a noticeable value only in the two regions symmetrically distributed apart from the axis defined by the metal wire. These two symmetric patterns start from the wire end with tilt angles of approximately $\pm 40°$ with respect to the z-axis. The underlying shape of the field emission is thus a cone, as previously observed by Deibel *et al.*[35] for the total field. The same behavior is obtained here considering the transverse field only. Along the z-axis, a modulation of the measured E_y-field intensity can be seen. This is a spurious effect caused by the metallic mount of the analyzer that reflects the output radiation from the wire-based antenna. As a consequence, artifactual standing waves of period $\lambda/2=1.5$ mm are visible in the image.

As previously observed in the far field,[36] the measured electric field shape looks like that of long-wire antennas. For tilt observation angles to the wire axis less than $\pi/2$, the theoretical far-field emission of resonant and traveling-wave type long-wire antennas may not be distinguished.[37] Both exhibit a first main lobe along the wire axis and subsequent secondary lobes with amplitudes that decrease very rapidly for long antennas. This main lobe is theoretically located at an angle of $\alpha=\cos^{-1}[1-0.371(\lambda/L)]$.[36,37] The present observation is, however, in the near field, and the measured $\approx 40°$ angle deviation of these lobes is far larger than the value of 7.8° expected for the tilt angle of the first main lobe of a 40λ traveling-wave wire antenna. Moreover, a care analysis of Fig. 2(c) indicates that the generating angle of the emission cone tends to reduce as the beam propagates. This illustrates the beginning of the near-field to far-field transition that is restricted here to the $[0,3\lambda]$ range. One can easily anticipate that for larger z the maximum far-field emission continues to elongate toward the z wire axis and results in a maximum emission much closer to the expected far-field emission of a long-wire antenna. From a near-field point of view, this measurement shows that the emission is predominantly due to the last few millimeters of the open wire. If the traveling-wave long-wire antenna model have to be used to explain the 40° tilt angle of the near-field emission, the corresponding active part of the wire antenna length should be less than 2λ. Our probe antenna may thus be viewed as a waveguide propagating a wire mode up to its open end where standing waves are generated for the current, the very last of these current oscillations only contributing in turn to the generation of a subwavelength longitudinal dipolelike source just beneath the wire end. This near-field source of longitudinal electric field radiates in far field a radially polarized doughnut beam. It is well known that the far electric fields of oscillating dipoles are radially polarized in planes perpendicular to the dipole directions.[38] As applied to probes, this enhancement of the E_z-component at the wire open end is expected to be used for near-field imaging.[24,39] Note that the intrinsic properties of the analyzer do not allow for the complete near-field characterization of the longitudinal dipolelike source at the antenna end since the E_z-component along the wire cannot be collected.

IV. PROBE-TO-PROBE COUPLING

The emission and collection properties of the proposed near-field probe antenna are obtained from a probe-to-probe coupling experiment using two devices as described in Fig. 1. The first probe antenna (A1) works in emission mode whereas the second one (A2) is used in collection mode. A1 and A2 both consist of a 12 cm long tungsten rod of 0.6 mm

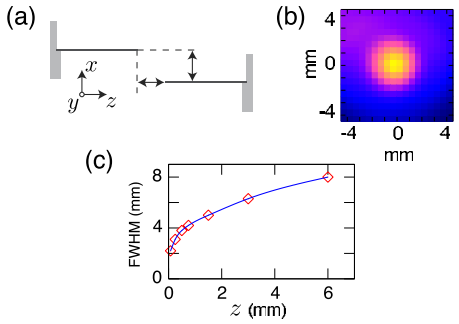

FIG. 3. (Color online) Probe-to-probe coupling experiment. (a) Experimental arrangement. The left probe is illuminated by the 0.1 THz source using parabolic mirrors. The output of the right probe is feed in a rectangular horn coupled to a WR10 waveguide that includes the Schottky diode detector. For convenience in the scheme, the two Teflon DPEs are represented with the same orientation although in practice they were $\pi/2$-cross-oriented to reduce the direct transmission. (b) Coupled power as measured in the (x,y)-plane normal to the wire at $z \approx 0$. (c) x-direction FWHM of the transmitted power as measured for various distances z between the two probes.

diameter connected to the properly designed DPE. While illuminating A1 with a collimated 0.1 THz beam, the transmitted power at the A2 output is detected using the Schottky diode receptor fed by a WR10 waveguide matched with a rectangular horn.

With the two tungsten wires brought in front at a distance of $\approx \lambda/10$, the 3D output near field of A1 is mapped by scanning the transverse (x,y)-plane over a zone of a few millimeter square around the radiating wire [see Fig. 3(a)]. The acquisition given with A2 [Fig. 3(b)] is totally different from the ones obtained with the analyzer at similar distances [Figs. 2(a) and 2(b)]. It exhibits a bright central spot with a maximum when the two wires are perfectly aligned. At first glance, it seems that A2 collects selectively the longitudinal electric field, which is missing in the images carried out with the analyzer. This is verified separately by calculating the electric field obtained at a distance $z=0.25$ mm of the wire end using the commercial finite-difference time-domain (FDTD) software "CST MICROWAVE STUDIO."[40] The calculated field profiles are given in Fig. 4(a). The longitudinal component is strongly enhanced at the wire apex while the radial component is canceled. As one departs from the perfect wire alignment $x=0$, both components become of comparable amplitudes and extend over a large distance. This is a well-known limitation of the wire guide that was already pointed in the earliest attempts of application.[19] The 2D transverse distribution of the E_z-field magnitude is also simulated at the wire apex [see Fig. 4(b)]. Despite some differences in spot shape and contrast, a rather good relationship between experimental and theoretical results is obtained.

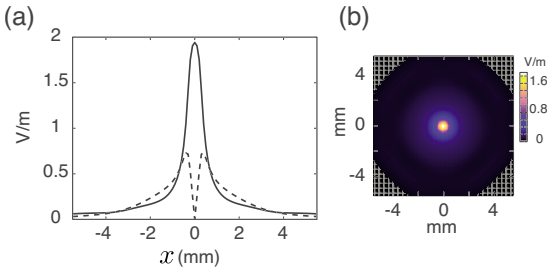

FIG. 4. (Color online) Calculated electric field magnitudes in a plane orthogonal to the wire and at the close distance $z=0.25$ mm. (a) Profiles of E_z (solid line) and E_r (dashed line). (b) Image of E_z.

More rigorously, the previous comparison between measurements and calculations is perturbed by image charge effects that are well known in SNOM, for example, with dipole emission near planar interfaces.[28] These effects may play a role when the two rods are very close, the field measured at the end of the wire being influenced by the wire itself. Nonetheless the measurement result given in Fig. 3(b) is the convolution of the emission and reception patterns of the two rods, thereby broadening and smoothing the rapid spatial variations of the field. The true transfer function from one probe to the other was not calculated using the FDTD method, an overlap integral method to be discussed later has been preferred. Perturbed fields were evaluated by FDTD calculations of the facing of two 0.6 mm diameter rods separated successively by distances of 0.5 and 0.2 mm. The results of Fig. 4 were compared with field amplitudes calculated in plans in between the two tips at $z=0.25$ mm and $z=0.1$ mm. At $z=0.25$ mm, the longitudinal field is lowered by a maximum of a few percent at the center and the radial component is enhanced by a similar amount, but the overall shapes of the field dependence with the radial coordinate remain unchanged and nearly indistinguishable from that of Fig. 4. Overall rms changes were evaluated to 0.8% and 0.6% for longitudinal and radial fields, respectively. If one reduces the distance to $z=0.1$ mm, the deviation obviously increases but remains low. At such a distance the image charge effects are thus not really negligible but the only visible difference is an enhancement of the field between the tips without important shape modifications on the electric field components. Since distances less than 0.25 mm were never considered with such probe, image charge effects can be neglected in the present results.

A complementary experimental analysis is conducted by registering similar images at various distances between the two wire ends [Fig. 3(c)]. On the one hand, it is straightforwardly observed that the maximum intensity detected at the perfect alignment position decreases exponentially when z increases. Such a result is in good agreement with the radiation properties of a longitudinally oriented dipole and will be illustrated in detail in the following with another probe (see Fig. 6). On the other hand, the spot size is also found to increase with z but following an evolution that is not dramatic. Starting from a spot with a full width at half maximum (FWHM) of $2\lambda/3$ close to the contact, the latter reaches 2λ when the two wires are separated by a distance of λ.

The comparison between Figs. 3 and 4 tends to confirm that a subwavelength longitudinal dipolelike source is induced at the wire end[24,39] despite the experimental spot size seems far larger than the theoretical one. The reason is that the calculated electric field does not match exactly the experimental configuration that involves a convolution between the two transfer functions of the emitting and detecting probes. A simple model of the probe-to-probe coupling is designed for a better interpretation of the experimental results. Let us consider $\mathbf{E}_1=\mathbf{E}(x,y)$ and $\mathbf{E}_2=\mathbf{E}(x-d,y)$, the

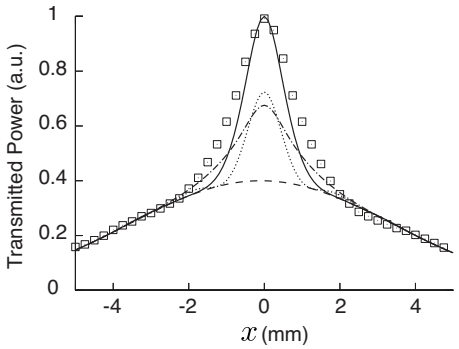

FIG. 5. Probe-to-probe transmitted power at the prescribed ($y=0$, $z=0.25$ mm) coordinate and as a function of the vertical displacement x. Squares are measurements and lines are calculations from Eq. (1) using as input the data of the FDTD calculations. Dash-dotted line: radial component alone. Dotted line: longitudinal component alone. Solid line: total field. Dashed line: Gaussian profile of the background noise contribution.

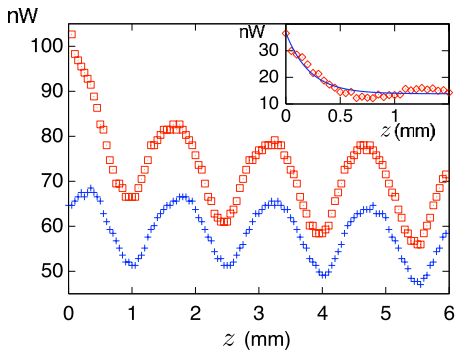

FIG. 6. (Color online) Probe-to-probe transmitted power as a function of the z-direction. The two identical probes use 4 cm long sharp needles. □, measured coupling between the two needles placed in front as a function of the distance z between them. +, same measurement with one needle removed. The inset gives the measured difference between previous data (◇) and gives a close view limited to $z \in [0, \lambda/2]$. Also plotted is an exponential fit (solid line).

fields at the outputs of A1 and A2 used in emission mode and collection mode, respectively. A2 is assumed identical to A1 but displaced by a distance d apart along the x axis. By analogy with fiber optics and using the output field vector $\mathbf{E}(x,y)$ obtained with previous FDTD calculations, the coupled power between A1 (emission) and A2 (collection) is obtained by the overlap integral[41]

$$P = \frac{\left|\iint \mathbf{E}_1 \cdot \mathbf{E}_2^* \mathrm{d}x\mathrm{d}y\right|^2}{\left|\iint \mathbf{E}_2 \cdot \mathbf{E}_2^* \mathrm{d}x\mathrm{d}y\right|}. \quad (1)$$

This model implicitly assumes a field vector $\mathbf{E}(x,y)$ emitted by the first antenna not perturbed by the second antenna. Although satisfactory for optical fibers, such an assumption is less sound here for antennas in the near field, but this approximation has the same physical foundation than neglecting image charge effects that we found reasonable with FDTD calculations.

Within this framework, transmitted powers are calculated and compared to the experimental data recorded by moving ±5 mm along the x-line of one probe with respect to the other one. Figure 5 plots the experimental results together with calculations obtained by considering successively only the longitudinal component $\mathbf{E}_z$, the radial component $\mathbf{E}_r$, and the total field. In practice the field of antenna A1 taken in Eq. (1) is always the total field $\mathbf{E}_1 = \mathbf{E}_r(x,y) + \mathbf{E}_z(x,y)$ whereas the field of antenna A2 is successively taken at $\mathbf{E}_2 = \mathbf{E}_r(x-d,y)$, $\mathbf{E}_2 = \mathbf{E}_z(x-d,y)$, and $\mathbf{E}_2 = \mathbf{E}_r(x-d,y) + \mathbf{E}_z(x-d,y)$. Because the two probe antennas are placed in front, the experiment also includes a background noise, even if the two DPEs have been $\pi/2$-cross-oriented to reduce the direct transmission between the emitting and detecting horns. This is practically accounted for in calculations by a Gaussian profile of width ≈10 mm added to the results of Eq. (1), in accordance with the 0.1 THz experimental beam waist. Obvious in Fig. 5 is the effect of the near-field components on the transmitted signal from A1 to A2 when x is small. At a larger separation between the two probe antennas, the transmitted power is mainly given by the direct throughput from the emitter to the receiver and is well described by the broad Gaussian profile. In the near field at the chosen distance $z=0.25$ mm considered here, each of the radial or longitudinal field shows a comparable effect, the detected signal from the radial field being nevertheless broader and lower than the detected signal from the longitudinal field alone. As a final comparison, an excellent agreement between theory and experiment is found when the total field is considered, the FWHM of the experimental transmitted power being slightly broader than the calculated one. This is probably because of the neglected coupling between the two probe antennas. Anyhow, it confirms the action of the dipolelike source at the wire end in the near-field image of Fig. 3(b), even if both the radial field and the far-field direct transmissions jointly act to reduce the contrast as compared to Fig. 4(b).

The previous probe-to-probe coupling experiment has shown that part of the transmitted power comes from the radial E-field component, thereby being understood just as the coupling between two facing long-wire antennas,[37] yet operating here in the near field. In order to obtain a clear evidence of the near-field coupling, we registered the intensity transferred from one probe to the other while increasing the distance between the two wires, starting from a position very close to the contact. In this experiment, the 12 cm long wires were replaced with two commercial needles of 4 cm long with very sharp spikes of ≈2 μm radius, as given by the manufacturer. It allows a closer positioning of the two probes with an estimated shorter available distance, given by the operator eye control only, that is estimated to a few tens of microns. As a rough rule of thumb drawn from the previous analysis on image charge effects, no major perturbations are thus expected with these tapered tips at any of the separation distances considered because all are far greater than the tip radius. We can then ignore the image charge effects for tip to tip interactions. Experimental results are given in Fig. 6 with the squares. Starting from the shortest estimated distance, the detected intensity first shows a rapid decrease and then an oscillatory behavior. The latter is induced by standing waves of observed period $\lambda/2 = 1.5$ mm generated in the Fabry–Perot resonator made by the two Teflon disks facing up. This effect has already been observed in probe-to-probe transfer characteristic,[12] although it was of far less

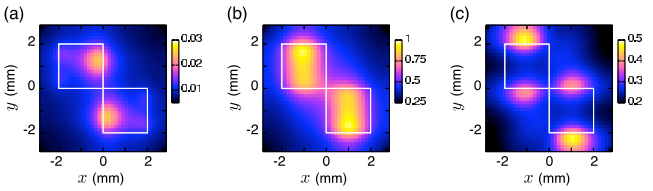

FIG. 7. (Color online) Calculated intensities of the electric field vector components as transmitted through the subwavelength square holes whose imprints are drawn in white for convenience. (a) E_x^2, (b) E_y^2, and (c) E_z^2.

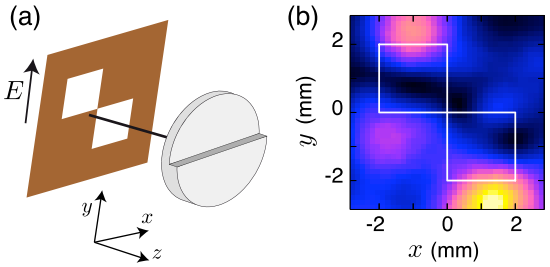

FIG. 8. (Color online) Near-field imaging of subwavelength square holes in a thin metal film. (a) Experimental arrangement. (b) Near-field intensity acquisition.

intensity. We separately investigated other configurations using the two 12 cm long tungsten wires instead of the needles. The relative importance and contrast of standing waves were found highly reduced, probably because of the three times longer Fabry–Perot cavity that induces much more important diffraction losses.

To proceed further with the two sharp needles, the standing waves were subsequently characterized simply by repeating the experiment with one needle removed. The obtained data shown with crosses in Fig. 6 exactly reproduce the previously observed oscillatory behavior. At short distances, measurements reveal, however, distinct features. The difference between the two measurements is shown in the inset and depicts an enhancement of the transmission near the contact that is well fitted by an exponential. This is the fingerprint of a near-field interaction between the two probes.

V. COLLECTION MODE: IMAGING SUBWAVELENGTH SQUARE HOLES

To confirm the ability of our probe antenna to collect locally E_z, we chose another source object to be imaged in the near field. Subwavelength square holes of 2×2 mm^2 size sharing one corner were opened in a thin metal sheet using laser trimming. This test object is illuminated on its backside at 0.1 THz with an input polarization along the y-axis parallel to some of the square edges [see Fig. 8(a)]. Incident radiations are concentrated on the sample zone with a parabolic mirror properly set in the illumination path. The simulation of the 3D field diffracted by the sample, in a plane at 0.25 mm from the surface, has been carried out with a FDTD method.[40] The results given in Fig. 7 show the intensity distributions of the three components of the diffracted electric field. As seen, the sample object is able to generate all three components of the electric field, the longitudinal one belonging only to the near-field zone because it does not propagate. The E_x-component that is orthogonal to the illumination polarization along y is weaker by two orders of magnitude as compared to the E_y- and E_z-components that are found of comparable intensities. More interesting is the observation that the transverse near-field components are mostly located at the center of the apertures whereas the longitudinal one is enhanced at the horizontal rims. It should be noticed that the calculated relative spot intensities depend on the flyover distance that was chosen in Fig. 7 to correspond with the average experimental to be used later. For instance, if the flyover distance is increased in calculations, the brightness of the two spots attached to the $y=\pm2$ mm square edges increases, whereas the brightness of the two spots attached to the $y=0$ mm square edges decreases. The spatial variations of the field components are only slightly subwavelength because the sample was designed to match the enhanced field area sizes with the 0.6 mm wire diameter of the probe, the sole purpose of this sample being to generate all three E-field components with balanced magnitudes when illuminated by a linearly polarized beam. This deliberate choice is intended to prove the selective capture of the longitudinal field by our probe, and its subsequent transfer by a Sommerfeld wire mode up to its radiation in the far field and detection, but not to show the ultimate achievable resolution of the system.

Figure 8(b) gives the image obtained when scanning the sample in the close neighborhood of its surface with the 12 cm long tungsten wire probe of 0.6 mm diameter. Enhanced field intensities are found over the metal along the horizontal rims of both squares, and no field is observed inside the holes. The nonperfectly central symmetric image observed here is assumed to be due to the metal foil that is not rigorously plane, mainly because of the mechanical and thermal constraints brought by the laser trimming. As a result, the average flyover distance is estimated to be about 0.25 mm on the average but with noticeable fluctuations that influence the near-field detection.

By comparing Figs. 8(b) and 7, one can see a good relationship between the experimental image and the calculated intensity E_z^2. This tends to prove that the proposed probe antenna collects mainly the longitudinal component of the electric field in the near zone. The capture of the longitudinal field in time-domain terahertz near-field measurements was shown only recently by Awad *et al.*[24] The E_z-component is measured only at micron distances that match their tapered tip end radius and is supplemented by an important background brought by the transverse field. Such a feature does not appear in Fig. 8(b) whereas Fig. 7(b) predicts an intense transverse field in the middle of the holes. The higher rejection of the transverse field found in our case is attributed to the detection that is performed only after the DPE and is then theoretically insensitive to any linearly polarized background.

Similarly to probe-to-probe coupling, the comparison between measurements and calculations may be perturbed by image charge effects that play a role when the probe is close to the metallic surface of the sample. Perturbed fields were evaluated by FDTD calculations including the probe above the metallic sample at a distance $z=0.25$ mm. The E_z^2-field

intensity in the middle of the probe-sample distance was calculated and compared to Fig. 7(c) as a function of the probe position. Indeed image charge effects modify the E_z-field distribution in between the sample and the probe, but this remains weak and occurs only in areas were high field intensity was calculated [see Fig. 7(c)]. The field intensity under the probe is approximately unchanged for $z=0.25$ mm. Since these are the data measured by the probe, no dramatic change can arise in the final image when charge effects are included. A care inspection of the numerical results based on many simulations lets only suggest that these effects induce a marginal expansion of less than 10% of the measured spots around the edges of the square holes.

VI. CONCLUSION

A passive probe antenna dedicated to cw near-field microscopy at millimeter and submillimeter wavelengths has been proposed. The probe function is achieved at the open end of a bare metal wire supporting Sommerfeld waves. The present probe differs from previous works in its original metal wire excitation system. Taking benefit from the cw operating regime, a discontinuous phase plate has been used to excite the metal wire waveguide from a linearly polarized beam propagating in free space, and vice versa, with a coupling efficiency theoretically estimated to 40%. This original antenna concept has been validated with a preliminary realization working at 0.1 THz.

A complete characterization of the probe antenna in the near-field zone and in the near-field to far-field transition has been carried out for the various vector components of the electric field. While going toward the far field, the emission involved mostly the radial polarization of the electric field with patterns approaching those of a long-wire antenna. In the near field, however, images of subwavelength square holes have shown that the probe antenna is predominantly sensitive to the longitudinal electric component. Another experimental setup with the aim of micron resolution and higher frequency operation is to being built to demonstrate in a forthcoming publication the high-resolution capability of this probe in the near field.

ACKNOWLEDGMENTS

The authors acknowledge L. Furfaro for the sample fabrication by laser machining at MIMENTO technology platform. This work is supported by the Agence Nationale de la Recherche under Contract No. ANR06-BLAN-0073. One of the authors (R.A.) also thanks jointly the CNRS and the Région Languedoc-Roussillon for doctoral fellowship.

[1] B. B. Hu and M. C. Nuss, Opt. Lett. **20**, 1716 (1995).
[2] *Sensing With Terahertz Radiation*, edited by D. Mittleman (Springer, Berlin, 2003).
[3] H. Chen, R. Kersting, and G. Cho, Appl. Phys. Lett. **83**, 3009 (2003).
[4] A. J. Huber, F. Keilmann, J. Wittborn, J. Aizpurua, and R. Hillenbrand, Nano Lett. **8**, 3766 (2008).
[5] M. Brehm, T. Taubner, R. Hillenbrand, and F. Keilmann, Nano Lett. **6**, 1307 (2006).
[6] K. Ishihara, K. Ohashi, T. Ikari, H. Minamide, H. Yokoyama, J. I. Shikata, and H. Ito, Appl. Phys. Lett. **89**, 201120 (2006).
[7] K. Iwami, T. Ono, and M. Esashi, Jpn. J. Appl. Phys. **47**, 8095 (2008).
[8] Y. Kawano and K. Ishibashi, Nat. Photonics **2**, 618 (2008).
[9] K. G. Lee, H. W. Kihm, J. E. Kihm, W. J. Choi, H. Kim, C. Ropers, D. J. Park, Y. C. Yoon, S. B. Choi, D. H. Woo, J. Kim, B. Lee, Q. H. Park, C. Lienau, and D. S. Kim, Nat. Photonics **1**, 53 (2007).
[10] F. Keilmann, Infrared Phys. Technol. **36**, 217 (1995).
[11] N. Klein, P. Lahl, U. Poppe, F. Kadlec, and P. Kuzel, J. Appl. Phys. **98**, 014910 (2005).
[12] E. Kume and S. Sakai, J. Appl. Phys. **99**, 056105 (2006).
[13] R. Lecaque, S. Gresillon, N. Barbey, R. Peretti, J. Rivoal, and C. Boccara, Opt. Commun. **262**, 125 (2006).
[14] N. van der Valk and P. Planken, Appl. Phys. Lett. **81**, 1558 (2002).
[15] A. J. L. Adam, N. C. J. van der Valk, and P. C. M. Planken, J. Opt. Soc. Am. B **24**, 1080 (2007).
[16] B. Gompf, N. Gebert, H. Heer, and M. Dressel, Appl. Phys. Lett. **90**, 082104 (2007).
[17] L. Meignien, J. Mangeney, P. Crozat, L. Duvillaret, and M. Hanna, Appl. Phys. Lett. **92**, 131103 (2008).
[18] A. J. L. Adam, J. M. Brok, M. A. Seo, K. J. Ahn, D. S. Kim, J. H. Kang, Q. H. Park, M. Nagel, and P. C. M. Planken, Opt. Express **16**, 7407 (2008).
[19] G. Goubau, J. Appl. Phys. **21**, 1119 (1950).
[20] H. Liang, S. Ruan, and M. Zhang, Opt. Express **16**, 18241 (2008).
[21] X.-Y. He, J. Opt. Soc. Am. B **26**, A23 (2009).
[22] R. Mendis and D. Grischkowsky, IEEE Microw. Wirel. Compon. Lett. **11**, 444 (2001).
[23] K. Wang and D. Mittleman, Nature (London) **432**, 376 (2004).
[24] M. Awad, M. Nagel, and H. Kurz, Appl. Phys. Lett. **94**, 051107 (2009).
[25] T. Jeon and D. Grischkowsky, Appl. Phys. Lett. **85**, 6092 (2004).
[26] T. Jeon, J. Zhang, and D. Grischkowsky, Appl. Phys. Lett. **86**, 161904 (2005).
[27] J. Deibel, M. Escarra, and D. Mittleman, Electron. Lett. **41**, 226 (2005).
[28] L. Novotny and B. Hecht, *Principles of Nano-Optics* (Cambridge University Press, Cambridge, 2006).
[29] Q. Zhan, Adv. Opt. Photonics **1**, 1 (2009).
[30] T. Grosjean, F. Baida, R. Adam, J.-P. Guillet, L. Billot, P. Nouvel, J. Torres, A. Penarier, D. Charraut, and L. Chusseau, Opt. Express **16**, 18895 (2008).
[31] Y. B. Ji, E. S. Lee, J. S. Jang, and T.-I. Jeon, Opt. Express **16**, 271 (2008).
[32] M. I. Stockman, Phys. Rev. Lett. **93**, 137404 (2004).
[33] S. A. Maier, S. R. Andrews, L. Martin-Moreno, and F. J. Garcia-Vidal, Phys. Rev. Lett. **97**, 176805 (2006).
[34] M. Berta, P. Kužel, and F. Kadlec, J. Phys. D: Appl. Phys. **42**, 155501 (2009).
[35] J. A. Deibel, N. Berndsen, K. Wang, D. M. Mittleman, N. C. J. van der Valk, and P. C. M. Planken, Opt. Express **14**, 8772 (2006).
[36] M. Walther, G. S. Chambers, Z. G. Liu, M. R. Freeman, and F. A. Hegmann, J. Opt. Soc. Am. B **22**, 2357 (2005).
[37] C. A. Balanis, *Antenna Theory—Analysis and Design*, 2nd ed. (Wiley, New York, 1982).
[38] J. D. Jackson, *Classical Electrodynamics*, 3rd ed. (Wiley, New York, 1998).
[39] R. Adam, J.-P. Guillet, L. Chusseau, A. Penarier, P. Nouvel, J. Torres, T. Grosjean, L. Billot, F. Baida, and D. Charraut, in EOS Annual Meeting—Topical Meeting on Terahertz Science and Technology, Paris, 2008, edited by P. Planken and M. Koch (unpublished).
[40] Computer Simulation Technology, http://www.cst.com/.
[41] J. Arnaud, *Beam and Fiber Optics* (Academic, New York, 1976).